Light Water Reactor Sustainability Program

Lower Length Scale Model Development for Embrittlement of Reactor Pressure Vessel Steel

Yongfeng Zhang
Pritam Chakraborty
Xianming Bai
Daniel Schwen

September 2016

DOE Office of Nuclear Energy

Light Water Reactor Sustainability Program

Lower Length Scale Model Development for Embrittlement of Reactor Pressure Vessel Steel

Yongfeng Zhang
Pritam Chakraborty
Xianming Bai
Daniel Schwen

September 2016

Idaho National Laboratory
Idaho Falls, Idaho 83415

http://www.inl.gov/lwrs

ABSTRACT

This report summarizes the lower-length-scale effort during FY 2016 in developing mesoscale capabilities for microstructure evolution, plasticity and fracture in reactor pressure vessel steels. During operation, reactor pressure vessels are subject to hardening and embrittlement caused by irradiation induced defect accumulation and irradiation enhanced solute precipitation. Both defect production and solute precipitation start from the atomic scale, and manifest their eventual effects as degradation in engineering scale properties. To predict the property degradation, multiscale modeling and simulation are needed to deal with the microstructure evolution, and to link the microstructure feature to material properties. In this report, the development of mesoscale capabilities for defect accumulation and solute precipitation are summarized. A crystal plasticity model to capture defect-dislocation interaction and a damage model for cleavage micro-crack propagation is also provided.

CONTENTS

FIGURES

ACRONYMS

AKMC	atomic kinetic Monte Carlo
APT	atom probe tomography
BWR	boiling water reactor
CD	cluster dynamics
CDM	continuum damage mechnics
CPFEM	crystal plasticity finite element method
CRP	copper rich precipitate
DD	dislocation dynamics
DFT	density functional theory
dpa	displacement per atom
FE	finite element
FP3DM	Frenkel pair three-dimensional diffusion model
MD	molecular dynamics
MNP	Mn/Ni rich precipitate
ODE	ordinary differential equation
PAS	positron annihilation spectroscopy
PDE	partial differential equation
PF	phase field
PWR	pressurized water reactor
RPV	reactor pressure vessel
RT	rate theory
SPPARKS	Stochastic Parallel PARticle Kinetic Simulator
TEM	transmission electron microscopy

1 Introduction

Maintaining the integrity of reactor pressure vessels (RPVs) is important for safe life extension of existing reactor fleets since they house the reactor core and internals, and are expensive to be replaced. During service, RPVs experience elevated pressure and temperature as well as neutron irradiation. For instance, in light water reactors (LWRs), RPVs usually operate at a temperature close to 300°C, and are exposed to neutron fluxes (E>1.0 MeV) in the range of 10^{12} to 10^{15} n/(m^{2}s), corresponding to atomic displacement rates in the range of 10^{-9} to 10^{-11} dpa/s [5]. Here dpa stands for displacement per atom. The flux is usually higher in pressurized water reactors (PWRs) than in boiling water reactors (BWRs). The exposure to high energy neutrons during irradiation causes the formation of lattice defects such as vacancies (unoccupied lattice sites) and interstitials (extra atoms on lattice sites) and their clusters. These defects diffuse at the high operating temperatures of RPVs, causing them to agglomerate and grow into extended defects such as voids, loops and other lattice defect features. These defects impede dislocation motion that leads to the hardening and embrittlement of RPVs [6], which can increase their propensity to fail. Moreover, the lattice defect features can enhance solute diffusion and significantly accelerate the precipitation process, leading to the formation of high densities of CRPs (Cu-rich precipitates) and MNPs (Mn/Ni-rich clusters), or, the so-called late-blooming-phases (LBPs). RPVs are typically made of iron-based steels, with Ni, Mn and Si being the primary alloying elements, and Cu as either an alloying element or an impurity [7]. Both CRPs and MNPs form in medium or high Cu-concentration (>0.1%Cu)) alloys, and only MNPs may form in low (or no) Cu-concentration (<0.1% Cu) alloys [1].

In order to reliably assess the safe life extension of existing reactors, quantitative correlation between irradiation dose levels, and hardening and embrittlement is needed at given operation conditions. The development of such correlation functions requires models or tools that can describe the evolution of RPV microstructure as irradiation goes on, because the mechanical properties are governed by the current microstructure. There are two physical processes, which are strongly coupled with each other, are responsible for hardening and embrittlement, and they are radiation damage accumulation and solute precipitation. The latter is usually accelerated by the former. However, due to the extremely slow kinetics involved in these two physical processes, and the long operational lifetime of RPVs, experimental determination of the correlation functions is extremely difficult. Hence, researchers have resorted to accelerated tests to obtain these correlations using fluxes with magnitudes higher than that experienced by RPVs in service in order to reach operational fluence levels at a much shorter time. However, the very different fluxes used in the test reactors from those in service may lead to very different microstructure evolution, resulting in inaccurate predictions of hardening and embrittlement. The use of surveillance data obtained from commercial reactors utilizing the same fluxes seems more realistic and accurate. Hence, these data have been used to fit and validate the semi-empirical engineering-scale models of RPV embrittlement [8, 9]. However, the extrapolation of these models to higher fluence levels that will be reached in extended reactor service life is questionable due to the missing physics. One key component missing in the previous correlations is there is no explicit consideration of MNPs or LBPs, because they are not present with a high density during the designed reactor life, usually 40 years. However, they may induce significant hardening and embrittlement during extended service, and thus need to be considered in the correlational models. This issue can be addressed through the development of physics-based multiscale modeling with experimental validations and has been pursued under the Grizzly project.

In the multi-scale approach, the length scale of interest ranges from subnanometers, where lattice defects form, to few centimeters, which corresponds to the size of the fracture specimens. On the other hand, the time-scale ranges from picoseconds, which is related to primary knockout of atoms and Frenkel-pair generation, to the expected service life of RPVs in decades. Various models at different length and time scales are being coupled in the overall scheme to obtain the damaged microstructure, and, the subsequent hardening and failure strengths, under long-term operating conditions. For RPV steels, the most important

microstructural features are lattice features representing radiation damage and solute precipitates, including their volumetric density, size distribution, and spatial distribution. These microstructural features evolve with time, dependent on the irradiation and thermal histories. For lattice features, rate theory (RT) and cluster dynamics (CD) are used. Atomic kinetic Monte Carlo (AKMC) and phase field (PF) are used for solute precipitation. For both lattice features and solute precipitates, atomistic simulations such as molecular dynamics (MD) simulations and density functional theory (DFT) calculations are needed to obtain the required material parameters. In reality, the evolutions of lattice features and solute precipitates are coupled with each other, with the detailed interactions not fully clear at this time [10, 11]. Thus, they are treated separately initially and their correlation will be elucidated later on by coupling the different methods. The effect of irradiation-induced defects on solute precipitation is taken into consideration by using vacancy concentration dependent diffusivities for solute elements. The meso and specimen scale deformation and fracture behavior is being modeled using crystal plasticity, continuum damage mechanics and probabilistic cohesive zone models. Crystal plasticity and continuum damage mechanics is used at the polycrystalline length scale to quantify the effect of dislocation-defect interaction on the increase in yield strength, strain-hardening and micro-crack propagation. The probabilistic cohesive zone model can subsequently utilize the parameters obtained from the meso-scale models to evaluate the ductile-brittle transition temperature shifts for safety assessments of RPVs.

The development of these models spans multiple years. In this document, the effort made in FY16 is summarized. More detail on this ongoing effort can be found in the previous Grizzly reports [12, 13, 14].

2 Atomic kinetic Monte Carlo simulations of precipitation in realistic RPV steel alloys

2.1 Introduction

Two main changes in the microstructures of RPV steels are the accumulation of radiation damage and the precipitation of solute elements. RPV steels are low alloying steels usually with the tempered bainitic microstructure, which consists of dislocation-rich ferrite and cementite. In both modeling and experiments, ferritic model alloys with the body-center-cubic (bcc) crystal structure have been widely used to investigate the solute precipitation during both thermal aging and neutron irradiation. Depending on the types of reactors and/or the locations in RPVs, the compositions of RPV steels may vary in terms of the concentrations of alloying elements. According to the Cu content, RPV alloys are classified as high Cu alloys ($c_{Cu} \geq 0.1\%$) or low (no) Cu alloys ($c_{Cu} < 0.1\%$). In high Cu alloys, precipitates are mainly Cu rich precipitates (CRPs) which can occur under either thermal aging or irradiation. While in low Cu alloys, precipitates are primarily Mn-Ni-rich (MNPs). These precipitates are observed experimentally only after neutron irradiation at high fluence, and thus sometimes called late blooming phase (LBPs).

In previous years, an atomic kinetic Monte Carlo (AKMC) method has been developed for solute precipitation in RPV steels. The AKMC model was implemented into the SPPARKS simulation package [15, 12, 16, 14], and was coupled with phase field for coarsening of precipitates [14]. The details about the AKMC method can be reached in the previous reports [12, 16]. A brief introduction is given here. In the AKMC model, a predefined lattice is used to represent the matrix with a certain crystal structure. An occupation index is assigned to each lattice to represent the element occupying that site. For solid solution, alloying elements are randomly distributed on the lattice. Their diffusion is via switch with vacancies that are either thermal or produced by irradiation. This method is powerful for coherent precipitation of impurities or alloying elements when the solubility is exceeded. In previous years, the AKMC model has been demonstrated using FeCu model alloys [16]. The coupling between AKMC and phase field in 2D and 3D simulations has been realized for FeCu alloys as well [14]. In FY16, the coupling between AKMC and phase field has been extended to FeCuNi alloys. The efficiency was improved by optimizing the integration scheme in MOOSE. The AKMC model has also been applied to FeCuNiMnSi alloys to represent realistic RPV steels to investigate the effect of irradiation induced lattice defects on precipitation.

2.2 Coupling of AKMC and Phase field

In FY15, we have demonstrated the coupling between AKMC and Grizzly phase field using FeCu alloys. The coupling was successful for 2D and 3D simulations. However, the efficiency of Grizzly phase field simulations was found to be low due the integration scheme used and the way the natural logarithmic term was computed. The natural logarithmic term with respect to alloying concentration is generic for free energy models of alloys and contains singularity when the concentration is zero, which will be the case when the atomic concentration field from AKMC for dilute alloys is transferred into phase field. The high computational expense of those phase field simulations strongly limits the Grizzly capability for precipitate coarsening.

To improve the performance of the coupled approach, efforts have been made in FY16 to optimizing the preconditioning and integration scheme in MOOSE. Another effort made was to replace the national logarithmic using the `plog` function in MOOSE. The `plog` function uses a polynomial from a Taylor expansion to replace natural logarithmic and a constant cutoff, below which the contraction will be replaced by the cutoff. The usage of a cutoff may induce some errors, which is negligible when the cutoff is much lower than the alloying concentrations. As shown in Fig.1, nucleation of Cu precipitate is readily observable in AKMC simulations. After being transferred into phase field, coarsening of Cu precipitates takes place, shown by the disappearance of small Cu clusters and growth of large ones. Phase transformation also occurs in large

Cu precipitates, along with the formation of Ni rings around them. This result demonstrates that the coupled approach is successful for modeling precipitate coarsening and the concurrent phase transformation in Fe-CuNi alloys. In the future, it will be extended to include more alloying elements such as Mn. The efficiency will be improved further to allow for large scale simulations.
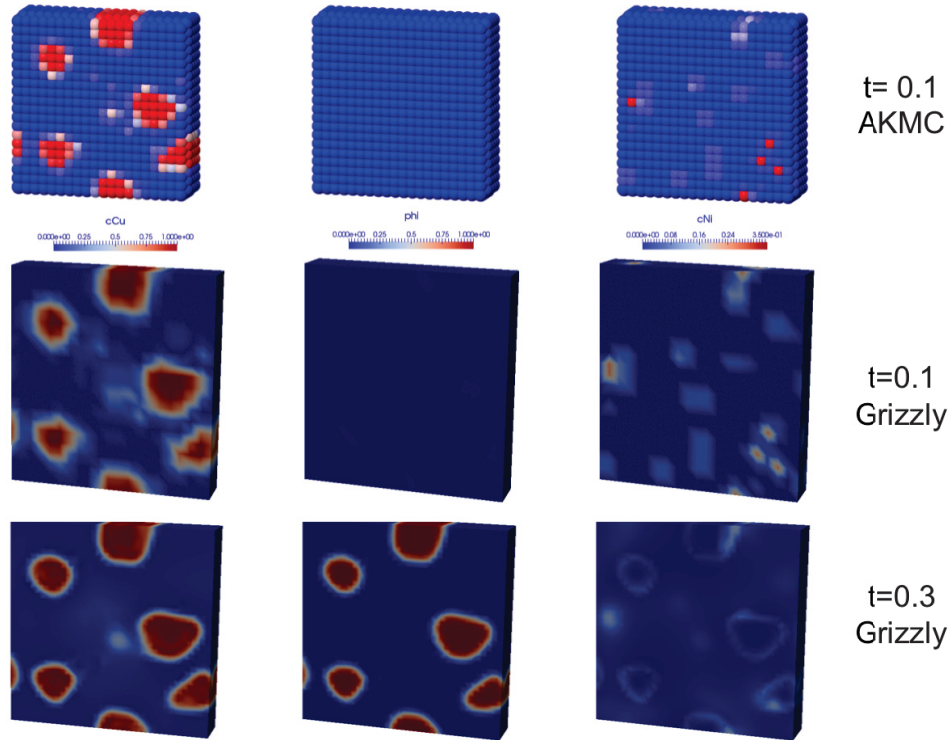
Figure 1: Precipitation of copper rich precipitates in a Fe15Cu1Ni alloy simulated by coupled AKMC (SP-PARKS) and phase field (Grizzly).

2.3   Precipitation in realistic RPV steels

In FY16, the AKMC model has also been applied to six FeCuNiMnSi model alloys to represent realistic RPV steels, where Ni, Mn and Si are the primary alloying elements, and Cu is either an alloying elements or an impurity. The concentrations of these alloying elements are taken as the same as those in several types of RPV steels [1], as shown in Fig.2. In the AKMC simulations, cubic simulation cells with 2 million atoms are used. The parameters given by Vincent et al. [17] are used to define the interatomic interaction, where the parameters were fitted using the results generated by density functional theory calculations. The bonding energies between vacancies are adjusted to give zero binding between them for the purpose of using multiple vacancies in the simulations to improve the efficiency. For thermal aging, the simulation cells are defect-free except for vacancies. For precipitation under irradiation, voids and interstitial loops are introduced to account for the effect of irradiation-induced precipitation. These two defect clusters have been widely characterized in irradiated RPV steels. As the AKMC method uses a rigid lattice, the interstitial loops are represented by their associated stress fields, which were found sufficient to describe the interaction with solute atoms [11]. For all simulations, a temperature of 573 K is used in accordance to RPV operation condition. The simulations last for 0.2 second in KMC time. Because the vacancy concentration used in AKMC is much higher than the thermal equilibrium concentration, 0.2 second in KMC time corresponds to a much longer realistic time, e.g. years, under thermal aging.

Nominal steel compositions (wt.%).								
Alloy	Cu	Ni	Mn	Mo	P	C	Si	Fe
LC	0.41	0.86	1.44	0.55	0.005	0.14	0.23	Bal.
LD	0.38	1.25	1.38	0.55	0.005	0.19	0.23	Bal.
LG	0.01	0.74	1.37	0.55	0.005	0.16	0.22	Bal.
LH	0.11	0.74	1.39	0.55	0.005	0.16	0.24	Bal.
LI	0.20	0.74	1.37	0.55	0.005	0.16	0.24	Bal.
CM6	0.02	1.68	1.50	0.54	0.007	0.15	0.17	Bal.

Figure 2: Chemical compositions of various types of RPV steels from Table 2 in Wells et al.[1].

Under thermal aging, it was found that the precipitation strongly depends on the amount of Cu. As shown in Fig.3, the number of clusters that formed in the six alloys studied decreases when the concentration of Cu decreases. Substantial precipitation is observed in only two alloys, LC and LD, both with high Cu concentrations. For alloys CM6 and LG, no precipitation takes place in 0.2 second (KMC time) due to the low Cu concentration. It should be mentioned that alloy CM6 has the highest Ni and Mn concentrations, without any precipitates observed in the AKMC simulation, indicating that MNPs, or LBPs, do not form under thermal aging in a time span comparable to reactor service life. This is in good agreement with experimental observations in the literature.
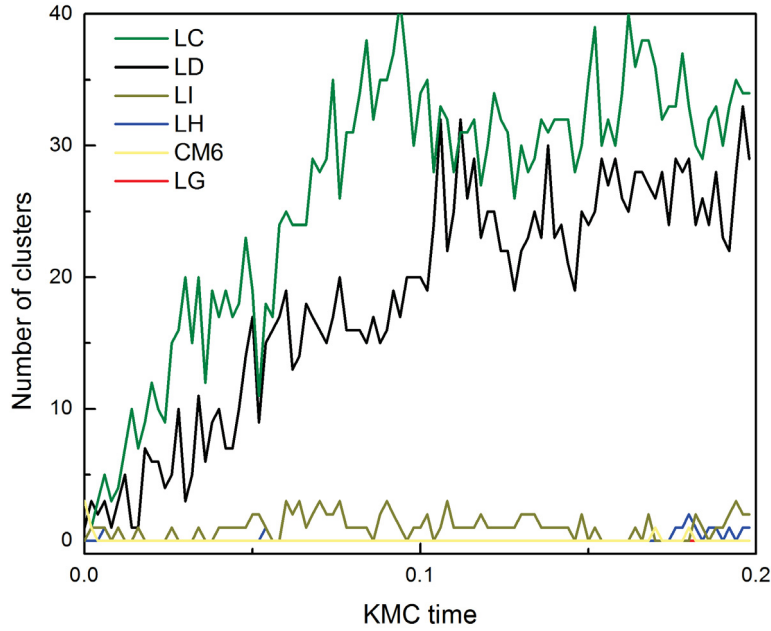
Figure 3: Numbers of solute clusters (precipitates) in six model alloys as functions of time from AKMC simulations.

In contrast to thermal aging, under neutron irradiation the presence of lattice defects may facilitate the precipitation of MNPs. As shown in Fig. 4, solute elements such as Ni, Si and Mn segregate at the surface of a void, 2 nm in diameter. Simulations with a smaller void show the same result. The segregation of these elements at void surfaces is primarily because of their high energies of mixing in Fe. This indicates that in irradiated RPV steels, MNPs can nucleate at small voids at high fluence. As for interstitial loops which

may attract solute atoms via the associated elastic stress field, no substantial segregation of Mn, Ni and Si is observed. The interaction of interstitial loops with solute atoms is dominated by elastic interaction. For Mn, Ni and Si, the interaction is weak and comparable to thermal noise, KT, at the RPV operation temperature. As a result, no strong segregation and precipitation take place at interstitial loops.
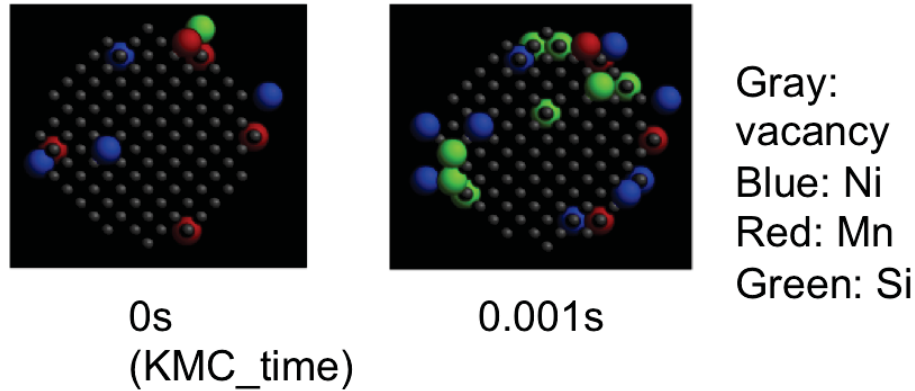
Figure 4: Segregation of Ni, Mn and Si to a void surface from AKMC simulations.

2.4   Summary

In summary, in FY16 the coupling between AKMC and phase field has been extended to FeCuNi alloys, and efficiency has been improved. The possible precipitation of MNPs in realistic RPV steels has been studied using AKMC. The results show that without Cu, MNPs either do not form, or form in a time span which is beyond the reactor design life time of 40 years during thermal aging. While under irradiation, their nucleation can be facilitated by the presence of voids or small vacancy clusters, in accordance to the observation of them in irradiated RPV steels at high neutron fluence. The results are qualitatively in line with previous understanding in the literature. In the future, coupling of AKMC, phase field with cluster dynamics will be carried out. From cluster dynamics, the amount of individual vacancies for enhanced diffusion and that of vacancy clusters for MNP nucleation will be extracted as inputs for AKMC/phase field simulations, in order to quantitatively predict the precipitation of solute elements under neutron irradiation.

3 Development of Cluster Dynamics Radiation Hardening and Radiation enhanced precipitation

RPV steels contain low concentrations of Cu either as an impurity or an alloy element [8]. Since Cu has a very low solubility in Fe, Cu can precipitate and form nanosized clusters during long-term thermal aging. In reactors, radiation can accelerate the Cu precipitation through the radiation-enhanced precipitation process. Cu precipitates can act as obstacles for dislocation motion. As a result, the yield strength of RPV steels increases (hardening) but the strain to failure decreases (embrittlement) [18], which is a potential safety concern for the lifetime extension of light water reactors.

In realistic RPV steels, the Cu concentration is very low, typically below 0.3 at.% [4]. The low solute concentration makes it challenging for modeling the precipitation of Cu clusters at long time. Cluster dynamics is a useful method to model the precipitation of low-concentration solute elements. It can model the nucleation, growth and coarsening of clusters in the same framework [19]. In FY16, a cluster dynamics model for the Cu precipitation in a low-Cu (0.3 at.%) steel under neutron irradiation has been developed. The predicted Cu cluster evolution kinetics such as cluster size distribution and number density are used as input in a dispersed barrier model to predict the increase of yield strength (hardening) due to the Cu cluster precipitation.

In cluster dynamics modeling [19], the number density of a cluster containing n Cu atoms is C_n. When a cluster of size n absorbs one Cu monomer, its size become $n + 1$. When a cluster of size $n + 1$ emits one Cu monomer, its size becomes n. Therefore, the flux from size n to $n + 1$ is:

$$J_{n \to n+1} = \beta_n C_1 C_n - \alpha_{n+1} C_{n+1} \tag{1}$$

where β_n is the absorption coefficient for a cluster of size n and α_{n+1} is the emission coefficient for a cluster of size $n + 1$. The absorption coefficient β_n is related to the radius of Cu atom (r_1), the radius of Cu cluster of size n (r_n), Cu diffusion coefficient (D_{Cu}), and the atomic volume of a bcc Cu atom (V_{at}),

$$\beta_n = 4\pi(r_1 + r_n)D_{Cu}/V_{at} \tag{2}$$

The two coefficients are related by the binding energy of the Cu cluster (E_b):

$$\alpha_{n+1} = \beta_n \exp\left(-\frac{E_b}{k_B T}\right) \tag{3}$$

The cluster binding energy is size dependent and has a close relation with the cluster interface energy. In this work the interface energy is set to 0.37 J/m^2. The binding energy increases with cluster size, as shown in Fig.5.

The time evolution of C_n is related to the fluxes of neighboring clusters,

$$\frac{dC_n}{dt} = J_{n-1 \to n} - J_{n \to n+1} \tag{4}$$

Therefore, by solving the differential equations of all clusters from size 1 to a maximum size n_{max}, the cluster size distribution (i.e., C_n vs. n) can be obtained at any given time. Using the cluster size distribution, the mean cluster size can be obtained.

When n_{max} is large, the efficiency of cluster dynamics is low because a total of n_{max} differential equations need to be solved at each time step. In order to improve the computational efficiency, the group method developed by Golubov et al. [20] has been implemented into our cluster dynamics modeling. The basic idea of the grouping method is to solve only two differential equations for a group of cluster sizes. Within each group, the cluster number density of each cluster size can be linearly interpolated based on the solutions
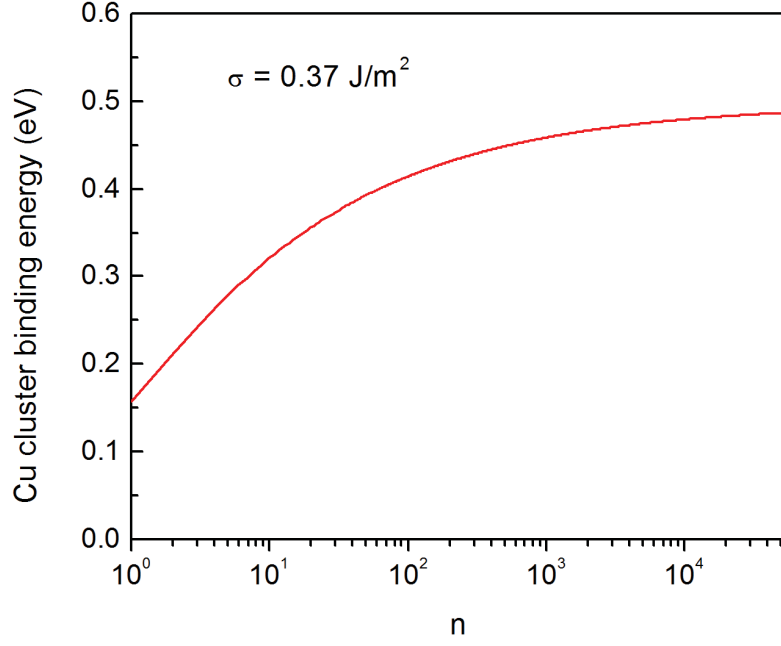
Figure 5: Size dependence of Cu cluster binding energy.

obtained from two differential equations. Using the grouping method, the number of differential equations can be reduced significantly and thus the efficiency is improved. Figure 6 compares the difference between the standard cluster dynamics simulation (no grouping) and the one with the grouping method. Clearly, the grouping method can produce identical results as the standard method but the computational time can be reduced by a factor of 400.
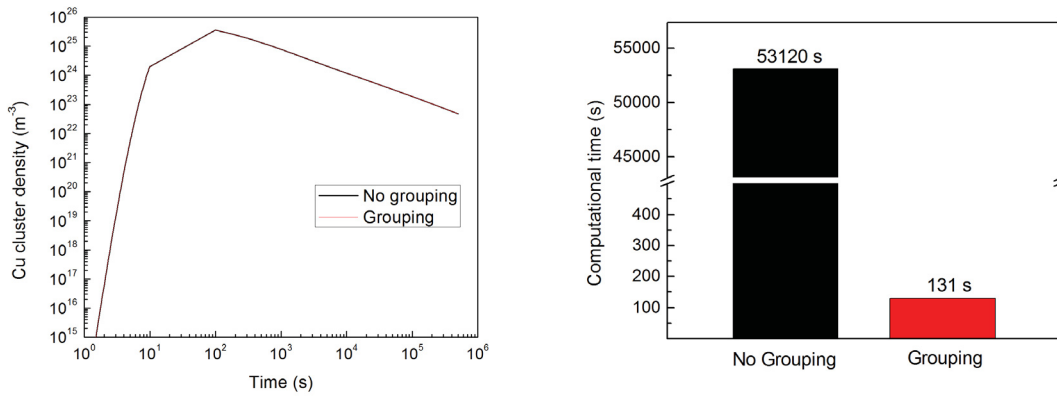
Figure 6: Comparison of the performance between cluster dynamics simulations with and without using the grouping method. (Left) The simulation using grouping method produces identical results as the simulation without using the grouping method. (Right) The computational efficiency is improved about 400 times by using the grouping method.

Since Cu atoms form substitutional defects in Fe, the diffusion of Cu atoms in a Fe matrix is mediated

by vacancies. For thermal aging, the thermal vacancy concentration determines the Cu diffusion coefficient. Under irradiation, the vacancy concentration can be much higher than the thermal vacancy concentration, in particular at low and moderate temperatures. As a result, Cu diffusion under irradiation is accelerated by irradiation. The radiation enhanced Cu diffusion coefficient is

$$D_{Cu}^{irr} = D_{Cu}^{th} \frac{C_v^{irr}}{C_v^{th}} \tag{5}$$

where the superscripts *th* and *irr* represent the thermal condition and irradiation condition, respectively, for vacancy concentration (C_v) and Cu diffusion coefficient (D_{Cu}). The thermal vacancy concentration is related to the vacancy formation energy in Fe and temperature, $C_v{}^{th} = \exp(-E_f/k_B T)$. Here, $E_f = 1.6$ eV is used. To calculate the vacancy concentration under irradiation ($C_v{}^{irr}$), a simplified rate theory model is used to describe the point defect evolution under irradiation. In this model, only defect production, defect recombination, and defect-dislocation interaction are considered. The time evolution of vacancy concentration (C_v) and interstitial concentration (C_i) are described by the following two equations [19],

$$\frac{dC_v}{dt} = \epsilon K_0 - k_{iv} C_i C_v - D_v C_v \rho_d \tag{6}$$

$$\frac{dC_i}{dt} = \epsilon K_0 - k_{iv} C_i C_v - D_i C_i \rho_d \tag{7}$$

where ϵ is the cascade efficiency; K_0 is the irradiation dose rate; k_{iv} is the defect recombination coefficient; D_v and D_i are vacancy and interstitial diffusion coefficients, respectively; ρ_d is dislocation density; and z_i = 1.2 is the dislocation bias factor so that dislocations absorb more interstitials than vacancies. By coupling the point defect evolution with Cu precipitation, the radiation-enhanced precipitation of Cu clusters can be modeled.

In this work, a cluster dynamics code was first developed to reproduce the published model of the radiation enhanced precipitation of Cu clusters in a Fe-1.34 at.%Cu alloy under electron irradiation, using the same parameters as in the literature [19]. Since electron irradiation only produces Frenkel pairs, the cascade efficiency is $\epsilon = 1$. The irradiation temperature is 290°C and the irradiation dose rate is 2×10^{-9} dpa/s. The dislocation density in the simulation is $\rho_d = 10^{12}$ m^{-2}. The copper migration barrier is 1.3 eV. At the steady state of point defect evolution, the radiation-enhanced factor for Cu diffusion is about 2.1×10^7, so that the precipitation kinetics is enhanced significantly by the irradiation. In the literature model, only the steady state value of the radiation-enhanced diffusion factor is used. In our work, the enhanced diffusion factor is directly coupled to the cluster dynamics modeling so that the radiation-enhanced diffusion effects can be captured more accurately, in particular at the transient regime before the defect evolution reaches the steady state. The modeling results are shown in Fig.7 . Results from the small-angle neutron scattering (SANS) experiments are also shown in Fig.7 for validating the model. For the evolution of cluster number density, a maximum value exists, indicating that Cu clusters undergo a transition from a nucleation and growth dominant regime to a coarsening dominant regime. The mean cluster size does not change much during the nucleation and growth regime but increases rapidly in the coarsening regime. The good agreement between cluster dynamics modeling and SANS experimental results indicates that the model works well for the radiation-induced precipitation under this irradiation condition.

In the electron irradiation experiment, the Cu concentration is 1.34 at.%, which is much higher than that in the realistic RPV steels (below 0.3 at.%). When the Cu concentration is low, precipitation kinetics is also very slow so that a longer simulation time or a higher irradiation dose is needed. Recently, Meslin et al. [4] have studied the precipitation kinetics of Cu clusters in an Fe-based alloy containing 0.3 at.% of Cu under neutron irradiation at 300°C. In their experiment, the neutron irradiation dose rate is about 1.4×10^{-7} dpa/s and the dislocation density in the alloy is about $\rho_d = 5\times10^{13}$ m^{-2}. To model the Cu precipitation for this
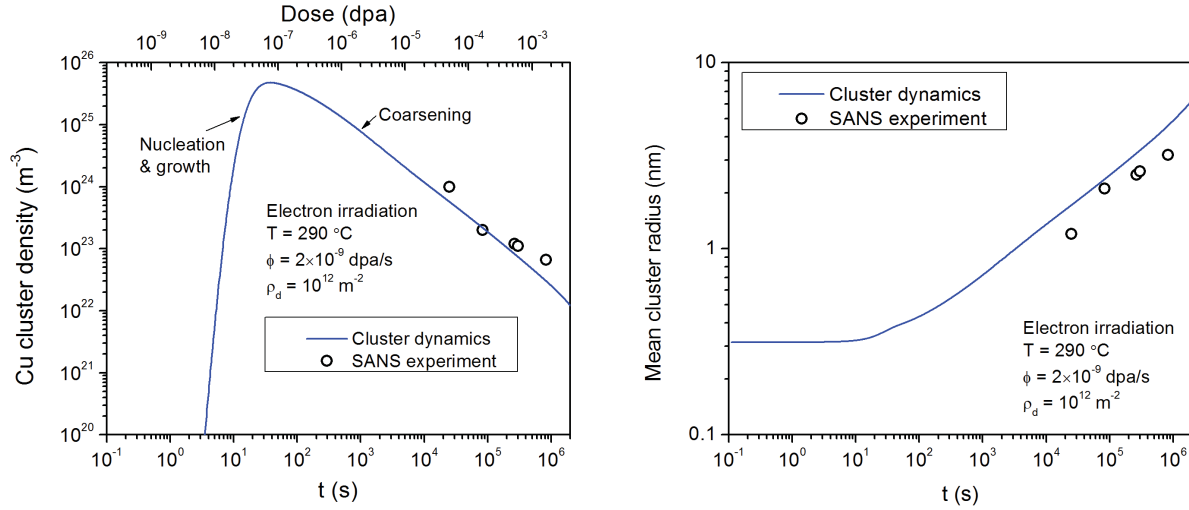
9

Figure 7: Cluster dynamics modeling of electron-radiation-enhanced precipitation of Cu clusters in a Fe-1.34 at.%Cu at 290°C. The modeling results (lines) are compared with the small-angle neutron scattering experiments (open circles). (Left) Evolution of Cu cluster number density as a function of irradiation time (or dose). (Right) Time evolution of the mean Cu cluster size.

experiment, we attempt to use the same parameter set as in the electron irradiation simulation, except for the material properties and irradiation conditions. However, our results show that the cluster dynamics modeling overpredicts the precipitation kinetics with respective to the experimental results. This discrepancy indicates that the model for the electron irradiation experiment cannot be directly applied to the neutron irradiation experiment. Therefore, some adjustment of the input parameters is needed.

Different from an electron irradiation in which only Frenkel pairs are produced and defect production efficiency is high ($\epsilon = 1$), neutron irradiation can produce collision cascades in which many displaced atoms can have in-cascade recombination. Thus, the cascade efficiency in neutron irradiation is lower than electron irradiation. Here we set $\epsilon = 0.4$ for neutron irradiation to capture the cascade effects. On the other hand, solute elements may interact with defects strongly and cause solute trapping effects on defect diffusion. It has been shown that Cu atoms and clusters can trap vacancies in the Fe matrix [21]. Since in the neutron irradiation experiment, the Cu concentration is much lower than in the electron irradiation experiment, it is reasonable to assume that the solute trapping effect on vacancy diffusion is weaker for the alloy with lower Cu content than higher Cu content. Therefore, in the simulation of neutron irradiation, the Cu migration barrier is decreased from 1.3 eV to 1.0 eV to reflect this solute trapping effect. Using the modified migration barrier, the enhanced factor for Cu diffusion decreases from 2.1×10^7 to about 7.7×10^5 at the steady state. Although this assumption is somewhat empirical, it does provide a reasonable justification for this parameter adjustment. For other parameters, they remain the same as in the electron irradiation simulation.

Using the modified parameter set, cluster dynamics simulations are conducted to calculate the evolution of Cu cluster number density and the mean cluster size at different neutron irradiation doses, as shown in Fig.8. The modeling results agree with experimental SANS measurement [4] very well for both cluster number density and mean radius. Compared to the electron irradiation simulation, the maximum cluster number density is about 23 times lower. The cluster coarsening also happens at much high dose range than in the electron irradiation.

The Cu precipitates can become obstacles for dislocation motion so that the yield strength of the alloy increases after the irradiation (hardening). To make the connection between the Cu precipitates and the hardening, a modified Orowan's looping model [22] is used. In this model, the increase of the shear strength ($\Delta\tau_s$) is related to the number density of Cu precipitates (N), the average diameter of the precipitates (d) with the following equation:

10
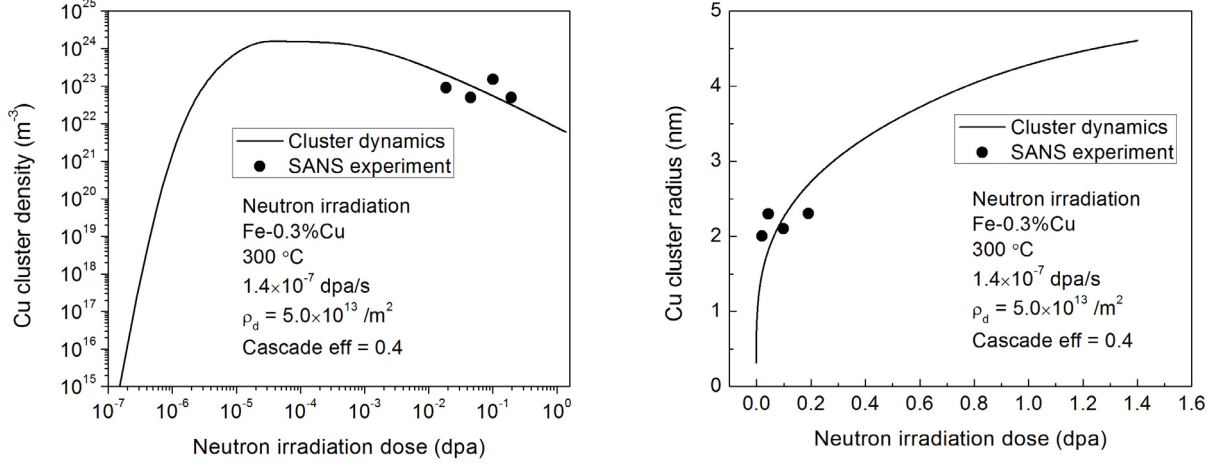
Figure 8: Cluster dynamics modeling of neutron-radiation-enhanced precipitation of Cu clusters in a Fe-0.3 at.%Cu at 300°C. The modeling results (lines) are compared with small-angle neutron scattering experiments (solid circles). (Left) Evolution of Cu cluster number density as a function of irradiation dose. (Right) The evolution of the mean Cu cluster size as a function of irradiation dose.

$$\Delta \tau_s = \alpha \frac{0.83\mu b}{[(Nd)^{-0.5} - d]} \cdot \frac{ln(d/r_0)}{2\pi(1-v)^{0.5}} \tag{8}$$

where α is the strength factor that is treated as size-dependent here; μ is the shear modulus of Fe matrix here and a value of 82 GPa is used here; b is Burgers vector of the <111>/2 dislocation; r_0 is dislocation core radius and here $r_0 = 3b$ is used; and v is the Poisson's ratio and here $v = 1/3$. The strength factor α changes from 0 to 1 as the cluster size increases. This size dependence captures the important physics that the obstacle is weak when a cluster is small while the obstacle is strong when a cluster is large. The increase of shear strength is correlated to the increase of yield strength by a Taylor's factor $M = 3.06$,

$$\Delta \sigma_y = M \Delta \tau_s \tag{9}$$

To calculate the increase in yield strength, two methods are used. In the first one, the total number density of Cu clusters and the average cluster diameter are used to calculate the effective hardening directly using Eqs.8 and 9. In the second method, the number density of each cluster size is used to calculate its individual contribution to hardening. The superposition law of square root of the quadratic sum is then used to calculate the total hardening:

$$\Delta \sigma_y = \sqrt{\Delta \sigma_1^2 + \sigma_2^2 + \sigma_3^2 + \cdots} \tag{10}$$

In experiments, the measured hardening includes the contribution from both Cu clusters and the Fe matrix defect clusters [3]. Therefore, a reverse superposition law is applied to extract the net contribution from Cu clusters:

$$\Delta_{Cu} = \sqrt{\Delta \sigma_{Fe-Cu}^2 - \sigma_{Fe}^2} \tag{11}$$

Using the cluster dynamics simulation results as input for Orowan's looping model, the evolution of radiation hardening can be calculated at different irradiation doses, as shown in Fig.9 . The hardening increases at low doses and reaches a saturated value at high doses. We find that the two ways of calculating the increase

of yield strength give very similar results, suggesting that the superposition law works very well in this work. The modeling results also have very good agreement with the experimental results [3], as shown in Fig.9.
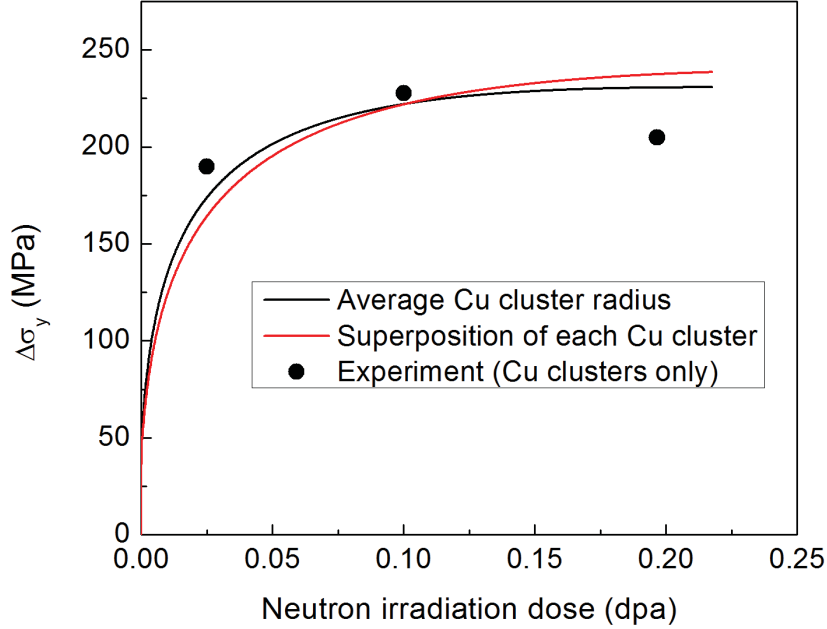
Figure 9: The Cu-cluster-induced hardening predicted by Orowan's looping model (lines), using the cluster dynamics simulation results of Cu precipitation as input. The two ways of calculating the hardening give similar results. The experimental results (filled circles) are also shown for comparison.

3.1 Summary

In summary, a cluster dynamics model has been developed to model the radiation-enhanced precipitation of Cu clusters in realistic (low-Cu) RPV steels under neutron irradiation. The modeling results have good agreement with the experimental measurement of Cu precipitation kinetics. Using a modified Orowan's looping model, the evolution of the radiation hardening due to Cu clusters at different irradiation doses is predicted and the modeling results have good agreement with experimental measurement.

The cluster dynamics model has been implemented as a standalone code solved by the Sundials solver. In the future, the model will be integrated to Grizzly either through linking to the PETSc solver or the Sundials solver in Moose framework. Currently the radiation hardening is predicted only based on Cu clusters. Under radiation, the Fe matrix in RPV steels can form many dislocation loops and voids. These matrix defects can cause additional radiation hardening as well. In the future, model development will include the contribution from Fe matrix defects as well.

4 Polycrystalline plasticity and damage models for irradiation induced embrittlement

The formation of irradiation induced defects such as self-interstitial atomic (SIA) loops, voids and precipitates, increases the long-term failure risks of RPV steels. The defects obstruct the motion of dislocations, thus hardening the matrix and reducing its ability to relax through plastic deformation. The effective stiffening of the material can lead to intergranular cracking and/or easier propagation of cleavage micro-cracks. Moreover, the precipitates and voids formed due to irradiation can act as micro-crack nucleation regions, thus increasing the propensity of failure. Hence, connecting the models of irradiation induced damage to deformation behavior at the microstructural scale is necessary to accurately quantify the embrittlement of RPV steels.

A dislocation-density based crystal plasticity model has already been implemented in Grizzly [13] to incorporate the effect of dislocations interacting with irradiation damage features in bcc systems. In the first-half of FY2016, the performance of this model has been evaluated against experimental data of yield stress and strain hardening/softening for iron and iron-copper systems [23]. This study is described in detail in Section 4.1.1. Further, the predictions from the crystal plasticity model have been compared in Section 4.1.2 with an analytical model of hardening. From these studies it can be seen that the crystal plasticity model is able to capture the defect-dislocation interaction at the polycrystalline length-scale quite satisfactorily.

In the second half of FY2016, efforts have been focused on coupling this validated meso-scale plasticity model to cleavage micro-crack propagation model. In bcc systems, the {100} and {110} are the cleavage planes for intragranular micro-crack propagation observed both experimentally and through atomistic simulations [24]. Though {100} planes are the relatively weaker ones, {110} planes can also fracture depending on the local stress state. The proposed model in this report attempts to incorporate the effect of all these planes on the cleavage fracture. A continuum damage mechanics (CDM) approach is pursued, where damage is evolved on these different planes through a constitutive law and the stress of the material is degraded using the damage variables. However, the difficulty of using the existing CDM based models for cleavage fracture stems from the non-orthogonality of the cleavage planes in bcc systems. Hence, a microplane model that can handle damage on the non-orthogonal cleavage planes to obtain the effective load carrying capacity of a material point is proposed in this report. The model has been implemented in Grizzly and is discussed in Section 4.2.

4.1 Comparison of the crystal plasticity model with experiments

Predictions from the crystal plasticity model have been compared with experiments for pure iron and iron-copper alloys. The defect densities and sizes under different irradiation conditions are obtained from [4] while the stress-strain responses are obtained from [2, 3]. Polycrystalline simulations are performed using Grizzly to calibrate the model parameters, which are subsequently validated. The predictions from the model are also compared with analytical equation of increase in yield strength at dpa levels for which the strain hardening/softening behavior is unavailable. The details of this study are described in Sections 4.1.1 and 4.1.2.

4.1.1 Calibration and validation of the model parameters for pure iron and iron-copper alloys

The stress-strain curves for the unirradiated and irradiated iron and iron-copper alloys provided in [2] are used to calibrate the model parameters. A representative volume of $500\mu m \times 500\mu m \times 500\mu m$ containing 64 cubic grains of size $125\mu m \times 125\mu m \times 125\mu m$ is considered for crystal plasticity finite element method

13

Table 1: Parameters of crystal plasticity model calibrated from tensile experiments on pure iron [2]

k_{mul}	0.28	k_{dyn}	15	q_p	0.07
q_i	0.046	β_i	0.4	η	5

(CPFEM) simulations. Each of the grains is associated with a single element and has a random orientation. Since the objective of these simulations is to evaluate the average response of the representative volume, such an approximation significantly reduces the computational cost while maintaining the desired accuracy. The representative volume is fixed along X, Y and Z directions on the back, left and bottom faces, respectively. The top face is displaced along the Z-direction with a strain rate of $10^{-4}/s$ to obtain the uniaxial stress-strain response of the representative volume. The FE discretized volume with the spatial distribution of one of the Euler angles and the boundary conditions are shown in Fig.10a and 10b, respectively.

(a)   (b)
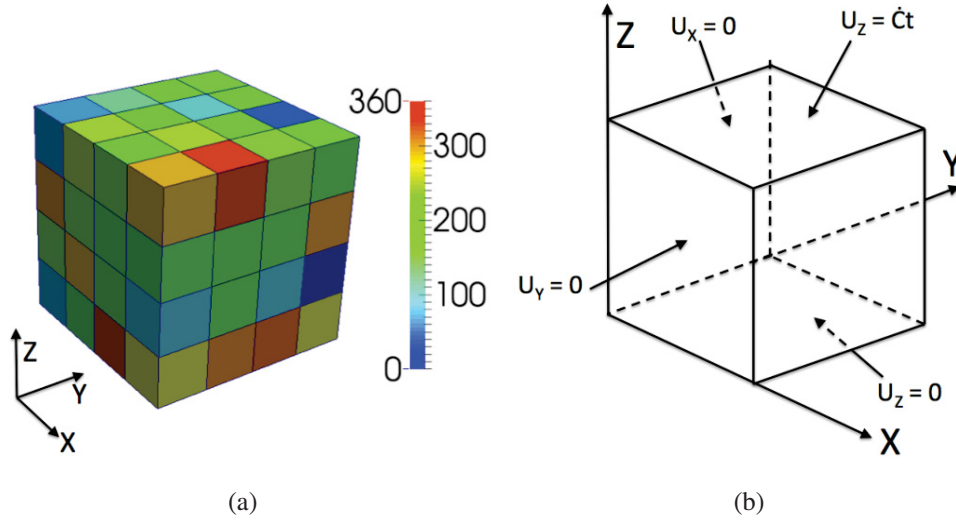
Figure 10: (a) The FE mesh and distribution of one of the Euler angles in the representative volume. (b) Boundary conditions to obtain uniaxial stress-strain response.

Most of the model parameters, apart from those involving defect terms, are first calibrated from the stress-strain curve of unirradiated pure iron. In the CPFEM simulations, mobile and immobile density values of 40 and 30 μm^{-2} are considered for pure iron, respectively, based on a total density of 70 ± 20 μm^{-2} reported in [2]. The neutron irradiation of pure iron to 0.1 dpa results in the formation of small vacancy clusters and $1/2 < 111 >$ SIA loops observed from transmission electron microscopy (TEM) and positron annihilation spectroscopy (PAS) analyses [3]. However, the vacancy clusters provide negligible resistance to dislocation motion due to their small size as compared to the much larger SIA loops. This has also been shown using the Orowan's strengthening model in [3]. Hence, based on this observation, only the SIA loop density and mean size information reported in [3] together with the stress-strain curve provided in [2] is used to calibrate the SIA loop related model parameters. The calibrated parameter values are shown in Table 1 and a comparison of the stress-strain curves is shown in Fig.11. Compared to dislocation dynamics (DD) [23], a significant lowering of dynamic recovery (k_{dyn}), barrier strengths (q_p, q_i) and loop annihilation (η) related parameters is necessary to match the experimental curves.

For the iron-copper alloys with 0.1% and 0.3% copper content, an increase in the post-yield hardening is observed in [2]. This trend is non-reproducible by simply incorporating the increased initial dislocation

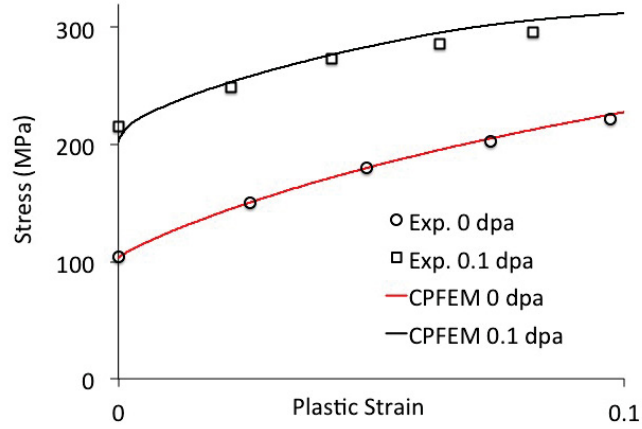Figure 11: Comparison of stress-strain evolution between CPFEM simulations and experiments [2] for unirradiated and irradiated pure iron.

Table 2: Defect density ($10^{20} m^{-3}$) and mean size (nm) values obtained from [3] used for calibration and validation of the crystal plasticity model

Alloy	Cluster Size	Cluster Density	Loop Size	Loop Density
Pure Iron	0	0	7	12.7
Iron 0.1% Cu	2.4	914	4.5	12.3
Iron 0.3% Cu	3	2177	5.2	35.5

densities of $90 \pm 20 \ \mu m^{-2}$ for these two alloys from [2]. As discussed in [25], the increase in hardening can be due to a higher dislocation multiplication promoted by the solute atoms. Considering this mechanism, the k_{mul} parameter is recalibrated from the experimental stress-strain curves for these alloys. The pinning of dislocations caused slight increase of yield stress, which is captured by modifying the barrier strength of iron 0.3% copper alloy. The following parameters are recalibrated for the two alloys: $k_{mul} = 0.32$ for iron 0.1% copper, and, $k_{mul} = 0.32$ and $q_p = 0.006$ for iron 0.3% copper. A comparison of the stress-strain curve with experiment is shown in Fig.12. In the CPFEM simulations, the mobile and immobile density values of 40 and 50 μm^{-2} are considered, respectively, based on a total density of $90 \pm 20 \ \mu m^{-2}$.

Under neutron irradiation to 0.1 dpa, small vacancy clusters, vacancy and copper clusters and SIA loops are observed in the iron-copper alloys, and are quantified using PAS, atom probe tomography (APT) and TEM measurements in [3]. Similar to pure iron, the small vacancy clusters provide negligible resistance, and the larger sized vacancy and copper clusters and SIA loops are the dominant barriers to dislocation motion [3]. Based on this observation, the crystal plasticity model parameters associated with the vacancy and copper clusters is calibrated using the experimental stress-strain curve for iron 0.1% copper provided in [2], and the cluster density and mean size information reported in [3]. With all other parameters remaining the same, $q_c = 0.02$ provided a satisfactory agreement with experimental stress-strain curve and is shown in Fig. 13.

The crystal plasticity model is subsequently validated for iron 0.3% copper using the defect density and mean size values provided in [3], and the corresponding stress-strain curve provided in [2]. A satisfactory agreement is obtained as can be observed from Fig.14. The defect density and mean size values obtained from [3] for pure iron and iron-copper alloys under neutron-irradiation to 0.1 dpa are listed in Table 2.

For the irradiated iron 0.3% copper alloy, the sensitivity of stress-strain evolution to the dislocation den-

15

Figure 12: Comparison of stress-strain evolution between crystal plasticity finite element method (CPFEM) simulations and experiments [2] for unirradiated iron-copper alloys.

Figure 13: Comparison of stress-strain evolution between crystal plasticity finite element method (CPFEM) simulations and experiments [2] for unirradiated and irradiated iron 0.1% copper alloy.
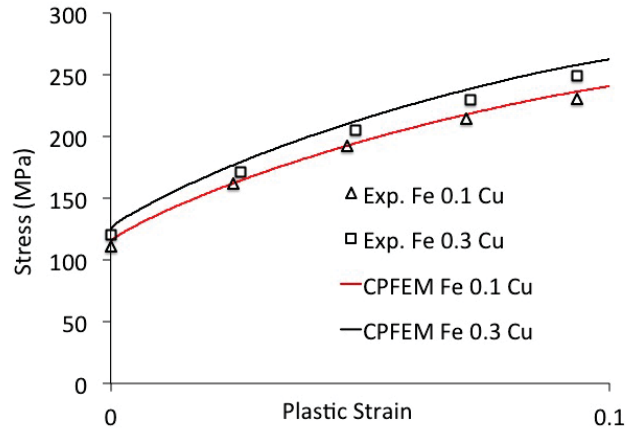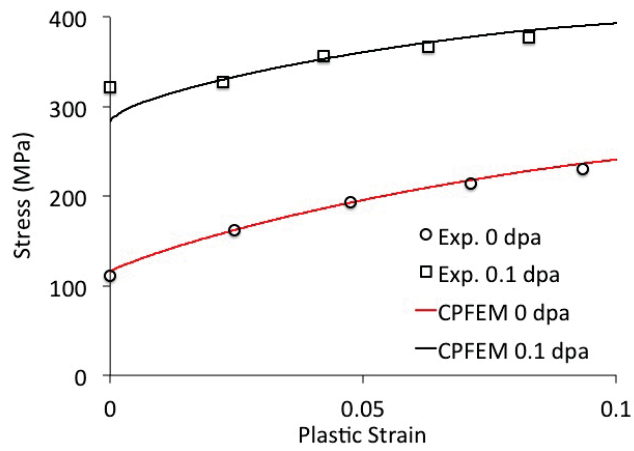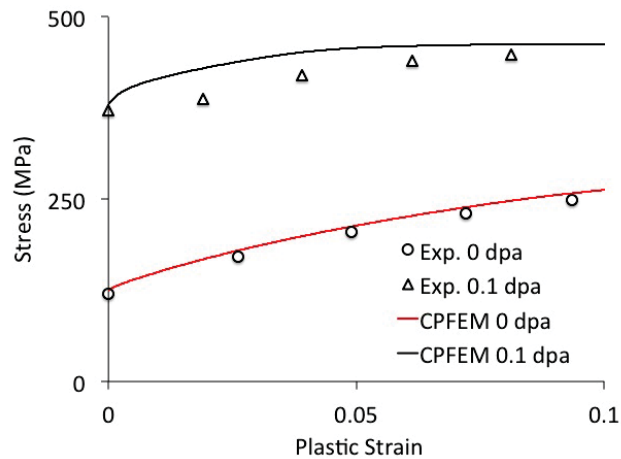

Figure 14: Comparison of stress-strain evolution between crystal plasticity finite element method (CPFEM) simulations and experiments [2] for unirradiated and irradiated iron 0.3% copper alloy.

sity and orientation distribution is further investigated. For the first case, the mobile and immobile dislocation densities are modified to 50 and 40 μm^{-2}, respectively, but the same random orientation of grains is maintained. For the second case, a different uniform random set of grain orientations is considered while the original mobile and immobile dislocation densities are utilized. The stress-strain evolution for these two cases is compared in Fig.15. As can be seen from the figure, a minor change in the stress-strain evolution occurs due to the variations in the mobile to immobile dislocation density ratio and orientation. This also shows that the number of grains considered in this study is reasonable to provide macroscopic flow-stress response from microstructure scale crystal plasticity simulations.
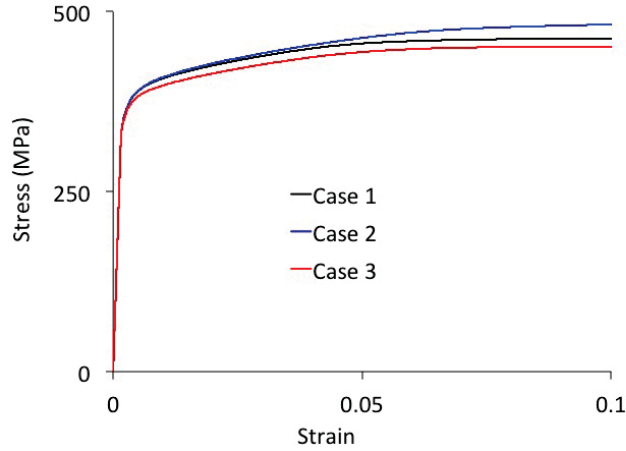

Figure 15: Sensitivity of stress-strain evolution to the dislocation density and orientation distribution for irradiated iron 0.3% copper alloy. Case 1: Original random orientation of grains with $\rho_M^\alpha = 40$ and $\rho_I^\alpha = 50$ μm^{-2}; Case 2: Original random orientation of grains with $\rho_M^\alpha = 50$ and $\rho_I^\alpha = 40$ μm^{-2}; Case 3: Different set of random grain orientation with $\rho_M^\alpha = 40$ and $\rho_I^\alpha = 50$ μm^{-2}. ρ_M^α and ρ_I^α are the mobile and immobile dislocation densities, respectively.

4.1.2   Comparison with an analytical hardening model

The influence of irradiation induced defects on the increase in yield stress is typically modeled using Orowan's strengthening model:

$$\Delta\sigma = \alpha M G b \sqrt{N d} \tag{12}$$

where α is the strength factor that depends on the defect type and size [22, 26], and, M is the Taylor factor. Eq.12 has been used in [3] to quantify the contribution of the different defect types such as clusters, precipitates and loops on the overall increase of yield strength for a RPV steel and its model alloys irradiated to 0.1 dpa. From their analyses it was shown that the small vacancy clusters have negligible influence on hardening. A decrease in the strength factor value (α) with reduction in mean defect size was obtained from their calibration as shown in Fig.16. However, an opposite trend was obtained for the vacancy-copper clusters as can be seen from the figure. Further, from their analyses it was concluded that a quadratic superposition of the resistances provided a better correlation with experimental results.

In the crystal plasticity model the same experimental data-set is utilized [3] for pure iron and iron-copper alloys. From a systematic calibration and validation process it is observed that constant barrier strength parameter (q_p, q_i and q_c) values is able to reproduce the experimental stress-strain response reasonably well within the range of mean defect size and density. This may be due to the consideration of a more detailed

interaction behavior between dislocation and defects in the crystal plasticity framework. Moreover, a linear superposition of the resistances is observed to be more suitable to model the increase in yield strength.

These two models are further compared by utilizing the microstructural information provided in [4] for pure iron and iron 0.1% copper alloy irradiated to different dose levels. Since the data provided for iron 0.3% copper alloy was incomplete, it could not be used in this comparative study. A comparison of the yield stress increase between the two models and experiments [3] is shown in Fig.17 and 18 for pure iron and iron 0.1% copper alloy, respectively. For pure iron irradiated to 0.05 dpa, both the models estimate a similar increase in yield strength (Fig.17b). At 0.2 dpa, both the defect density and mean size evolve significantly (Fig.17a) though the yield strength increase almost saturates (Fig.17b). However, by utilizing this defect information at 0.2 dpa both the models predict a higher increase of yield strength as compared to experiments, though the crystal model is closer to the experimental values (Fig.17b).

For the iron 0.1% copper alloy, the SIA loop density and mean size increase with dose level (as can be observed in Fig. 18a), though these increases are much less severe than for pure iron. Also, the vacancy-copper cluster mean size shows very little increase with dose, while the number density is even observed to decrease at 0.2 dpa. Based on this defect information, a much closer estimate of yield-strength increase is predicted from the models (Fig.18b). However, a saturation of yield-strength increase as seen in the experiment is still not obtained from both the crystal plasticity and analytical model. The results for the iron 0.1% copper alloy suggests that the defect mean size and density values at 0.2 dpa provided in [4] may require re-evaluation.

The stress-strain and strain-hardening behavior as obtained from the crystal plasticity model is compared in Fig.19. An insignificant change in the strain-hardening rate is observed until the engineering strain reaches 0.025 for all the dose levels. Beyond this strain level, a reduction in the strain-hardening rate is noticeable for 0.1 and 0.2 dpa, and is due to the increased annihilation of the SIA loops by the matrix dislocations. For pure iron irradiated to 0.2 dpa, a strain softening behavior can even be observed beyond 0.025 engineering strain. At strains lower than 0.025, a small increase in the strain-hardening rate can be observed for all the dose levels. This increase can be attributed to an increased trapping of dislocations by the SIA loops. A similar trend can be observed from Fig.20 in iron 0.1% copper alloy as well. For this alloy, the reduction in the strain-hardening rate is lower, however, than for pure iron since the primary softening mechanism is attributed to dislocation-SIA loop interaction in the model.
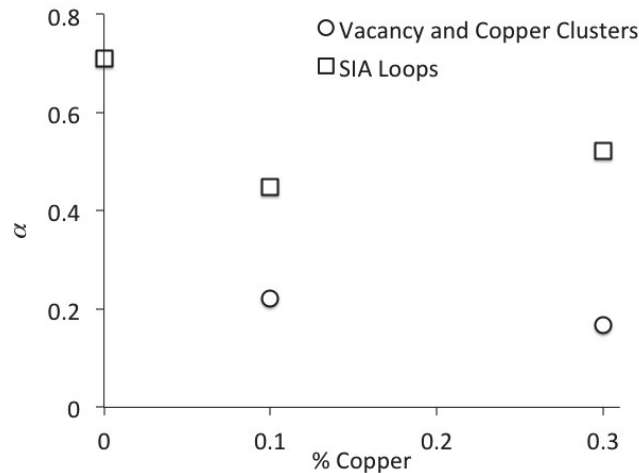
Figure 16: The variation of SIA loop and vacancy-copper cluster strengths (α in Eq.12) obtained in [3] for pure iron and iron-copper alloys.

18
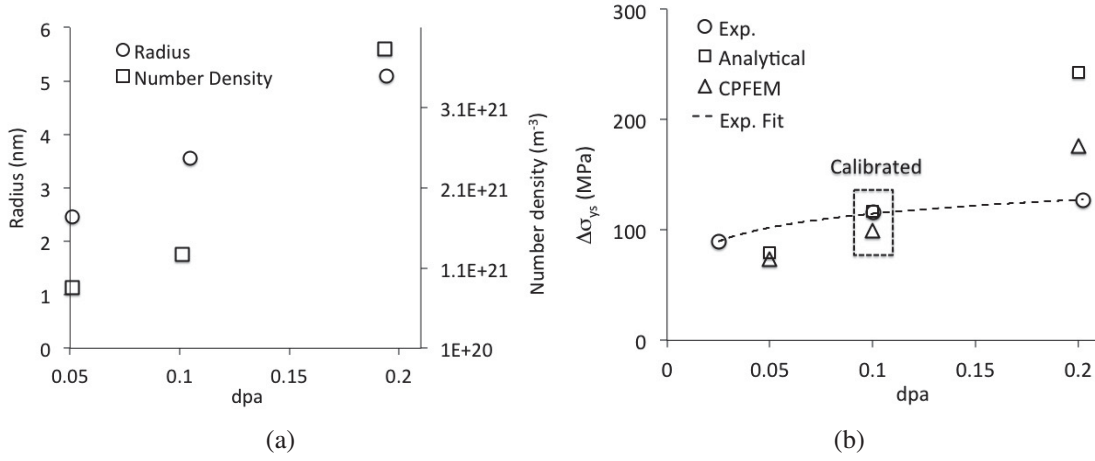
Figure 17: (a) Mean size and number density of SIA loops in pure iron irradiated to different dose levels [4]. (b) Comparison of increase in yield stress ($\Delta\sigma_{ys}$) obtained from crystal plasticity and analytical model.
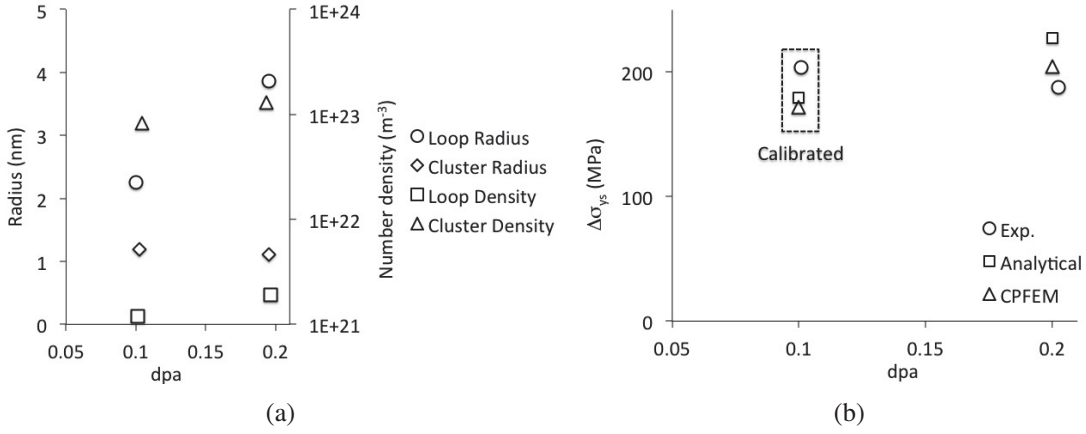
Figure 18: (a) Mean size and number density of SIA loops in pure iron irradiated to different dose levels [4]. (b) Comparison of increase in yield stress ($\Delta\sigma_{ys}$) obtained from crystal plasticity and analytical model.

Figure 19: Comparison of (a) stress-strain, and, (b) strain-hardening, evolution for pure iron irradiated to different dose levels obtained from crystal plasticity model.

Figure 20: Comparison of (a) stress-strain, and, (b) strain-hardening, evolution for iron 0.1% copper irradiated to different dose levels obtained from crystal plasticity model.

4.2 Microplane model for cleavage fracture

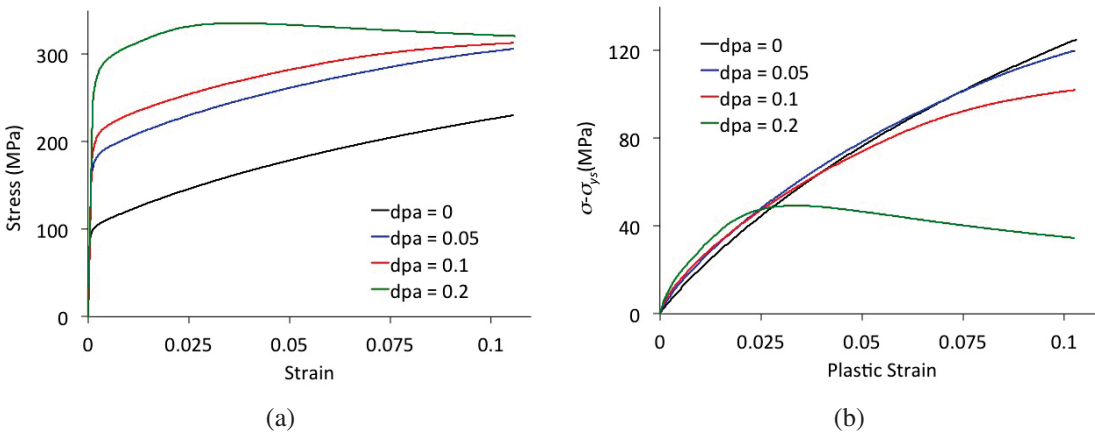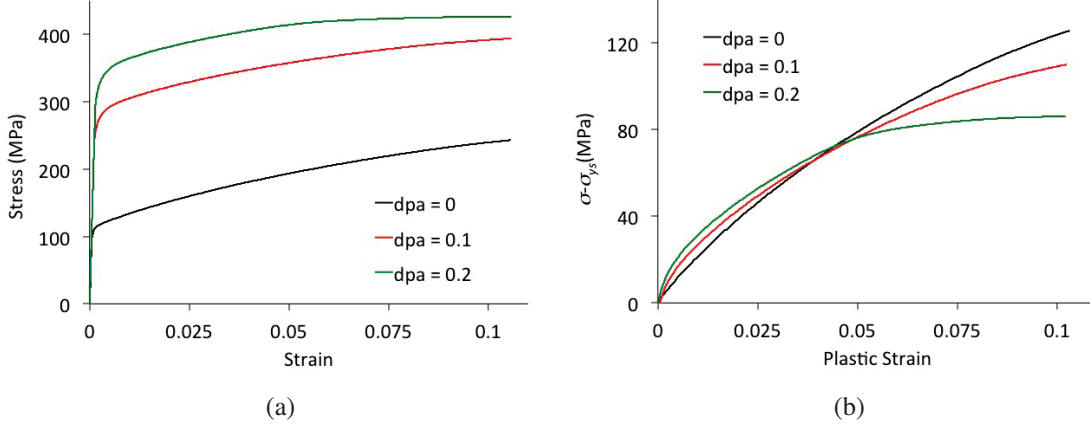Cleavage fracture in bcc systems occurs on specific planes in conjunction with crack-tip plasticity. Detailed atomistic simulations in [24] has shown that bond breaking, dislocation slip, and twin formations occur during crack propagation from a pre-existing flaw in bcc iron. The plastic deformation mechanism and the resulting stress-strain curve depend on the plane of the flaw and direction of propagation. From these simulations it is observed that cleavage failure on the $\{100\}$ planes require the least energy followed by $\{110\}$ planes. Dislocation slip and twin is more dominant on $\{111\}$ planes, which strongly retards cleavage crack propagation. From these observations $\{100\}$ and $\{110\}$ are considered as possible cleavage planes in this work.

To capture the coupled plasticity and cleavage crack growth in bcc iron, a microplane damage model in conjunction with crystal plasticity is currently being developed in Grizzly. The specific internal energy of the coupled model can be represented as

$$\psi = \psi_e + \psi_p \tag{13}$$

where the plastic energy rate can be related to slip on individual slip systems following

$$\dot{\psi}_p = \sum_\alpha \dot{\gamma}^\alpha \underline{\underline{S}}^\alpha_0 \tag{14}$$

and the elastic energy can be represented as

$$\psi_e = \frac{3}{2\pi} \int_\Omega \underline{t} \cdot \underline{e}^e d\Omega \tag{15}$$

In Eq. 14, $\dot{\gamma}^\alpha$ and $\underline{\underline{S}}^\alpha_0$ are the slip rate and Schmid tensor for slip system α, respectively. Eq. 15 is the microplane representation of elastic energy [27] where $\underline{t}$ and $\underline{e}^e$ are the projected stress and elastic strain respectively. Ω in Eq. 15 represents the unit-sphere over which the projected stresses and elastic strains are integrated. The projected stresses and strains are evaluated in the intermediate configuration following

$$\underline{v} = \underline{\underline{V}} \cdot \hat{n} \tag{16}$$

where $\underline{v}$ is the projected vector variable, $\underline{\underline{V}}$ is the corresponding tensor variable and $\hat{n}$ is the normal on the unit sphere. In the proposed model $\underline{e}^e$ and $\underline{t}$ are related to the elastic Lagrangian strain tensor ($\underline{\underline{E}}^e$) and 2nd

20

Piola-Kirchhoff stress tensor ($\underline{\underline{T}}$), respectively. The projected variables are further decomposed into normal and shear components as

$$\underline{v} = v_n \hat{n} + \underline{v}_s = \underline{\underline{N}} : \underline{\underline{V}}\hat{n} + \underline{\underline{T}} : \underline{\underline{V}} \tag{17}$$

where $\underline{\underline{N}} = \hat{n} \otimes \hat{n}$ and $\underline{\underline{T}} = \hat{n} \cdot \underline{\underline{I}} - \hat{n} \otimes \hat{n} \otimes \hat{n}$. For isotropic elasticity without damage, $\underline{t}$ can be related to $\underline{e}^e$ following

$$t_n = E_n e_n^e, \text{ and, } \underline{t}_s = E_s \underline{\underline{I}} : \underline{e}_s^e \tag{18}$$

where $E_n = 3K$ and $E_s = 10G/3 - 2K$ with K and G being the bulk and shear modulus respectively from [27].

Based on the general microplane theory, an isotropic and anisotropic microplane damage model has been implemented in Grizzly. In the isotropic damage model, a normal (d_n) and a shear (d_s) damage variable is considered for every microplane. Though in thoery this can lead to infinite number of variables, the numerical integration of the microplane model restricts the number of damage variables to the quadrature rule considered. As described in [27], the damaged elastic strain energy can then be represented as

$$\psi_e^m(\hat{n}) = (1 - d_n) \frac{1}{2} E_n \langle e_n^e \rangle_+^2 + \frac{1}{2} E_n \langle e_n^e \rangle_-^2 + (1 - d_s) \frac{1}{2} E_s e_s^e : \underline{\underline{I}} : e_s^e \tag{19}$$

where ψ_e^m is the elastic strain energy on every microplane and $< x >_\pm = (x \pm |x|)/2$. As can be observed from the equation, the normal damage variable only degrades the load carrying capacity of a microplane under tension, while a contact type behavior with the elastic stiffness is obtained under compressive projected normal strain. However, there is no directionality associated for the effect of damage on the shear deformation of a microplane. The evolution of damage is based on the projected elastic strain energy as

$$d_i = 1 - exp\left(-\left[\frac{\kappa_i}{a}\right]^p\right) \tag{20}$$

where a and p are the parameters of the damage model. The subscript i represents the damage law in normal (n) or shear (s) direction on a microplane. The damage history is maintained through

$$\kappa_i = \max_{0<s<t} \left(Y_i(s), \kappa_i\right) \tag{21}$$

where Y_i for damage in normal direction follows

$$Y_n = \frac{1}{2} E_n \langle e_n^e \rangle_+^2 \tag{22}$$

and in shear direction follows

$$Y_s = \frac{1}{2} E_s e_s^e : \underline{\underline{I}} : e_s^e \tag{23}$$

As can be observed from Eq.22, only separating projected strain along the normal direction of a microplane ($\langle e_n^e \rangle_+$) contributes to damage evolution.

In the anisotropic model, only normal separation of specific damage planes (d_n) are considered. Since, normal separation of planes can also reduce the shear resistance of a plane, the degraded elastic strain energy is represented as

$$\psi_e^m(\hat{n}) = (1 - d_n) \frac{1}{2} E_n \langle e_n^e \rangle_+^2 + \frac{1}{2} E_n \langle e_n^e \rangle_-^2 + (1 - d_n) \frac{1}{2} E_s e_s^e : \underline{\underline{I}} : e_s^e \tag{24}$$

21

As can be observed from Eq.24, only the normal damage variables on predefined planes are considered in this model. The evolution of d_n follows Eqs.21 and 22. The damage on the predefined planes can reduce the projected undamaged area on other planes where there is no explicit plane separation. To capture this effect Eq. is modified as

$$\psi_e^m(\hat{n}) = A_f \frac{1}{2} E_n \left\langle e_n^e \right\rangle_+^2 + \frac{1}{2} E_n \left\langle e_n^e \right\rangle_-^2 + A_f \frac{1}{2} E_s \underline{e}_s^e : \underline{\underline{I}} : \underline{e}_s^e \tag{25}$$

where

$$A_f = \prod_{i=1 \text{ to } n} \left(1 - d_i \left|\hat{n}_i \cdot \hat{n}\right|^m\right) \tag{26}$$

In Eq.26, n is the number of predefined damage planes and m is a parameter that determines the extent by which the damage area is projected. Further, in the anisotropic model the effect of crystal orientation is incorporated by evaluating the constitutive model in the material coordinate system followed by transformation to the global system. The rotation matrix for these transformations are formed using the Euler angles and discussed in [13].

4.2.1   Numerical integration of the microplane model

In the microplane model the projected stress and Jacobian needs to be integrated on the unit sphere to obtain the 2nd order stress and 4th order Jacobian tensor at any material point. This is accomplished by using Gauss-type quadratures and associated weights to obtain the desired accuracy. The 33-point rule provided in [28] is used in the present work to perform the integration. Due to the symmetricity of the stress tensor, the gauss-points and weights on a quarter of the sphere is only required.

4.2.2   Results and Discussion

The microplane model described in this report is tested using one element and 2-D plane-strain symmetric center-crack simulations. At first, the performance and accuracy of the model is tested for isotropic elasticity. A comparison of the stress-strain response between microplane and standard constitutive model for a unit-cube uniaxially displaced is shown in Fig.21. A satisfactory agreement is observed for this case.
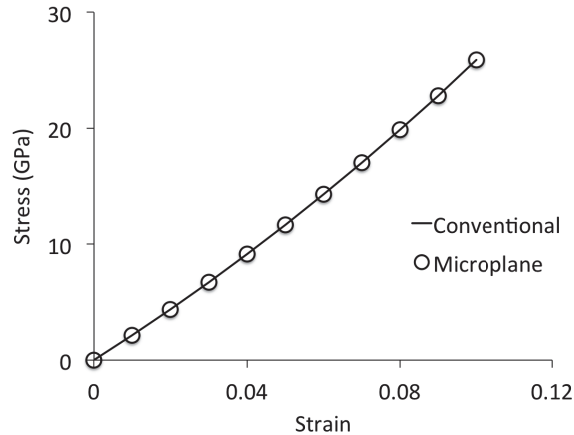

Figure 21: Comparison of stress-strain response between microplane and conventional isotropic elasticity model under uniaxial tension.

A one element 3D unit cube is uniaxially loaded along [001] direction under cyclic displacement to test the isotropic damage model. The temporal evolution of strain is shown in Fig.22a. Under this loading, (001) is the microplane of maximum damage and is depicted in Fig.22b. The model allows damage evolution only in tension and is evident from Fig.22b and Fig.22c. During unloading there is no damage evolution on the microplane and a contact type behavior is observable as shown in Fig.22c.
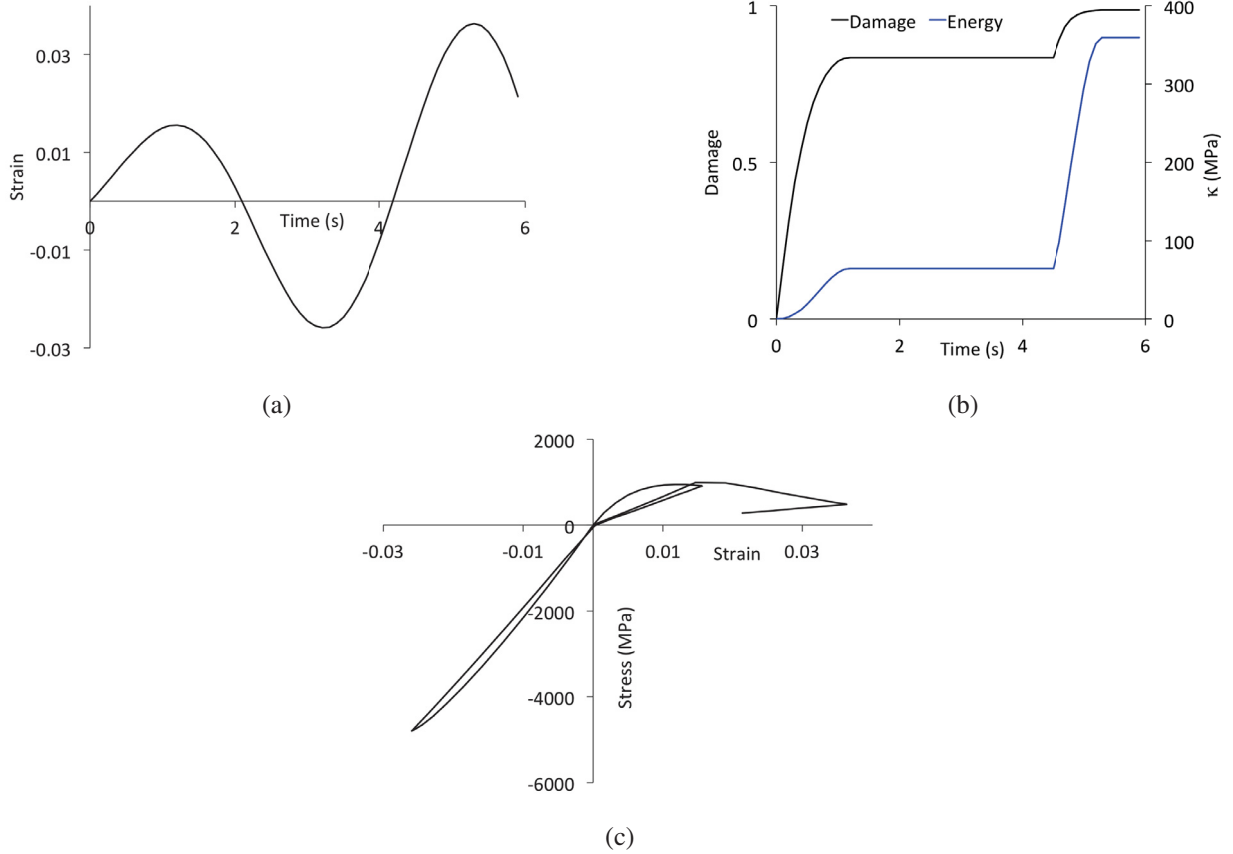

(a)

(b)

(c)

Figure 22: One element 3D unit cube simulation with isotropic damage. (a) Cyclic strain history; (b) Evolution of normal damage and the corresponding driving force on (001) plane; (c) Stress-strain evolution.

2D plane-strain symmetric center-crack simulations are performed to evaluate the performance of the anisotropic damage model. The finite element model and the boundary conditions are shown in Fig.23. Euler angles of (0 0 0) and (45 0 0) degrees are utilized to see the effect of crystal orientation on the stress-strain evolution. The {110} is assigned a higher critical energy to damage (a) than the {100} microplanes, for these simulations. Though a mode-I damage propagation is observed in both the cases, the maximum damage microplanes are different, viz. (010) and (110) for (0 0 0) and (45 0 0) Euler angles, respectively. The damaged configuration for the 2 cases are shown in Fig.24 and 25.

A comparison of the force-displacement behavior between the 2 cases is shown in Fig.26. As can be observed from the figure, the (45 0 0) orientation has a higher ultimate strength as compared to (0 0 0) orientation. This behavior also matches qualitatively with the MD simulations of [24].

4.3   Conclusion

The quantification of irradiation induced embrittlement of RPV steels requires the development of microstructure scale models that can couple grain-scale plasticity and fracture. Based on this objective, a
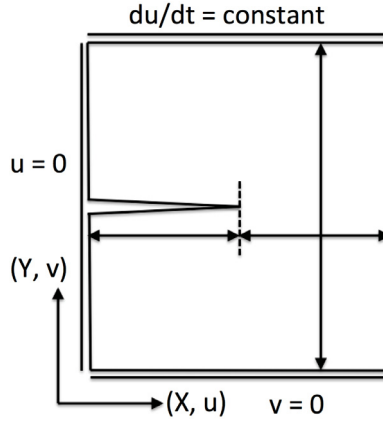
Figure 23: Finite element model and boundary conditions for the symmetric center crack specimen.

| (a) | (b) |

Figure 24: Damaged configuration in symmetric center-crack specimen for (0 0 0) crystal orientation. Damage on microplanes (a) (010) and (b) (110).

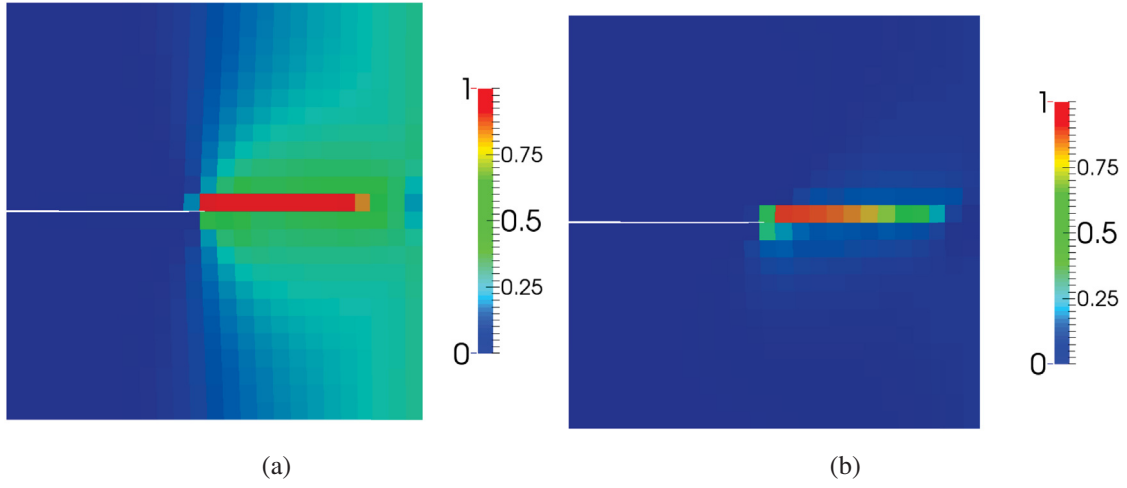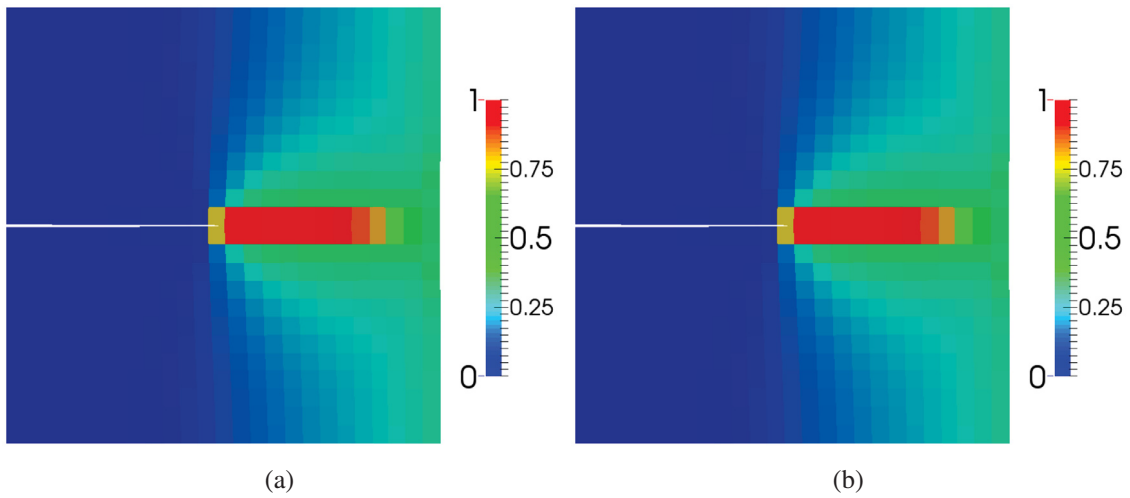| (a) | (b) |

Figure 25: Damaged configuration in symmetric center-crack specimen for (45 0 0) crystal orientation. Damage on microplanes (a) (110) and (b) (100).
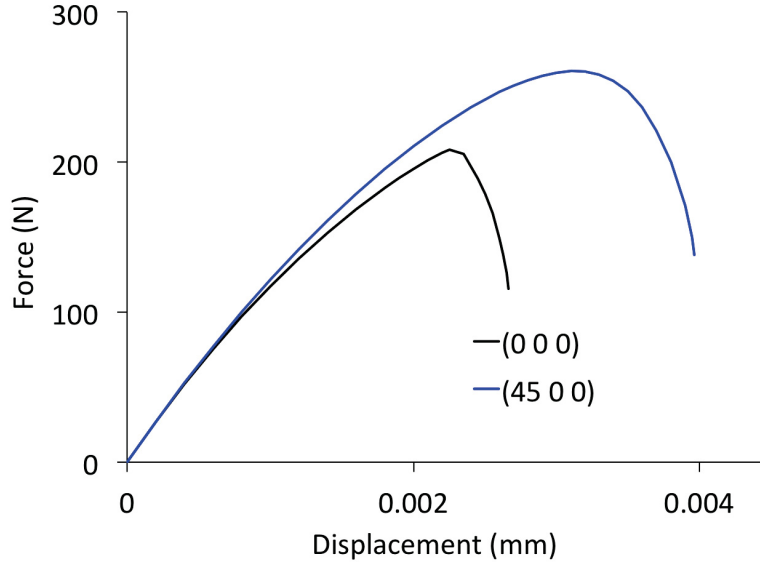
Figure 26: Force-displacement from the symmetric center crack simulations for the 2 different orientation.

crystal plasticity model was developed in FY2015 that can incorporate defect-dislocation interaction at the polycrystalline length-scale. This model has been validated using experimental data for unirradiated and irradiated iron and iron-copper in the first half of FY2016. From the validation study it can be observed that the model is able to predict the increase in yield strength and strain hardening satisfactorily.

In the second half of FY2016, a microplane damage model has been developed that can be coupled to the crystal plasticity model and capture anisotropic cleavage fracture in bcc systems. In the damage model, specific cleavage planes with different strength to failure can be specified leading to orientation dependent failure of the material. Both one element unit cube and 2D plane-strain symmetric center crack simulations have been performed to demonstrate the workability of the model. Satisfactory qualitative comparison with MD simulations can be obtained utilizing the microplane damage model.

5   Summary

In FY16, progress has been made in developing lower-length-scale models for microstructure evolution and property degradation in reactor pressure vessel steels. In previous years, an atomic kinetic Monte Carlo model has been developed and coupled with phase field for solute precipitation. A cluster dynamics model is being developed for radiation damage. For hardening and embrittlement, effort was made to assess the performance of the dislocation-density based crystal plasticity model developed in previous years, and to couple with with a cleavage micro-crack propagation model developed this year.

The accomplishments have increased the Grizzly capability for modeling microstructure evolution and property degradation, and also made broad impact in the research community. The research and development outcome has led to the publication of one journal publications and 6 presentations at leading conferences, including 5 invited talks, and one invited seminar at a university (listed below). The lower-length-scale capability has also led to the collaboration with a university professor in a NEUP preproposal currently being reviewed.

To continue this multiscale, science based approach, in FY17 attention will be paid to: 1) finishing the cluster dynamics model and implementing that model in Grizzly 2) coupling lattice kinetic Monte Carlo and phase field with cluster dynamics for precipitation in RPV steels under neutron irradiation; 3) transferring microstructure information to crystal plasticity and fracture mechanics for hardening and embrittlement.

Journal publications:

1. P. Chakraborty and S. B. Biner, Crystal plasticity modeling of irradiation effects on flow stress in pure-iron and iron-copper alloys, Mechanics of Materials 101, 71-80, 2016.

Invited talks:

1. Yongfeng Zhang, Daniel Schwen, Xianming Bai, Benjamin Spencer, Coupling Lattice Kinetic Monte Carlo and Phase Field for Solute Precipitation in RPV Steels, MRS-Spring 2016, Phoenix, AZ, March 2016

2. Pritam Chakraborty, Benjamin Spencer, Marie Backman, William Hoffman, Xian-Ming Bai, Yongfeng Zhang, Grizzly: A Multi-scale and Multi-Physics Tool to Model Aging of Nuclear Power Plant Components, ANS 2016, New Orleans, LA, June 2016

3. Yongfeng Zhang, Pritam Chakraborty, Daniel Schwen, Xianming Bai, Michael Tonks, Benjamin Spencer, Multiscale Modeling of Microstructure Evolution and Property Degradation in Reactor Pressure Vessels, MS&T 2015 Meeting, Columbus Ohio, October 2015

4. Daniel Schwen, Yongfeng Zhang, Rapid Development of Phase Field Models for RPV Aging, MS&T 2015 Meeting, Columbus Ohio, October 2015

5. Pritam Chakraborty, Yongfeng Zhang, Bulent Biner, A Crystal Plasticity Model to Investigate the Radiation Dose Dependent Flow Stress and Cleavage Behavior in RPV Steels, MS&T 2015 Meeting, Columbus Ohio, October 2015

6. Yongfeng Zhang, Daniel Schwen, Pritam Chakraborty, Xianming Bai and Benjamin Spencer, Multi-scale modeling of microstructure evolution in reactor pressure vessel steels, Graduate student seminar, Rensselaer Polytechnic Institute, October 2015

6 References

1. Peter B. Wells, Takuya Yamamoto, Brandon Miller, Tim Milot, James Cole, Yuan Wu, and G Robert Odette. Evolution of manganese-nickel-silicon-dominated phases in highly irradiated reactor pressure vessel steels. *Acta Mater.*, 80:205, 2014.

2. M. Lambrecht, L. Malerba, and A. Almazouzi. Influence of different checmical elements on irradiation-induced hardening embrittlement of RPV steels. *Journal of Nuclear Materials*, 378:282–290, 2008.

3. M. Lambrecht, E. Meslin, L. Malerba, M. Hernandez-Mayoral, F. Bergner, P. Pariege, B. Radiguet, and A. Almazouzi. On the correlation between irradiation-induced microstructural features and the hardening of reactor pressure vessel steels. *Journal of Nuclear Materials*, 406:84–89, 2010.

4. E. Meslin, M. Lambrecht, M. Hernandez-Mayoral, F. Bergner, L. Malerba, P. Pariege, B. Radiguet, A. Barbu, D. Gomez-Briceno, A. Ulbricht, and A. Almazouzi. Characterization of neutron-irradiated ferritic model alloys and a rpv steel from combined APT, SANS, TEM and PAS analyses. *Journal of Nuclear Materials*, 406:73–83, 2010.

5. R E Stoller. *The Effect of Neutron Flux on Radiation-Induced Embrittlement in Reactor Pressure Vessel Steels*. ASTM International, 2003.

6. D J Bacon, Y N Osetsky, and D Rodney. *Dislocation-Obstacle Interactions at the Atomic Level*, chapter 88. Elsevier, 2009.

7. G.R. Odette and G.E. Lucas. Embrittlement of nuclear reactor pressure vessels. *JOM*, 57:18–22, 2001.

8. C. English and J. Hyde. Radiation damage of reactor pressure vessel steels. *Comprehensive Nucl. Mater.*, 4:151–180, 2012.

9. E.D. Eason, G.R. Odette, R.K. Nanstad, and T. Yamamoto. A physically-based correlation of irradiation-induced transition temperature shifts for rpv steels. *J. Nucl. Mater.*, 433:240–254, 2013.

10. B. Radiguet, A. Barbu, and P. Pareige. Understanding of copper precipitation under electron or ion irradiations in fecu0.1 wt% ferritic alloy by combination of experiments and modelling. *J. Nucl. Mater.*, 360:104–117, 2007.

11. Yongfeng Zhang, Paul C. Millett, Michael R. Tonks, Xian-Ming Bai, and S. Bulent Biner. Preferential cu precipitation at extended defects in bcc fe: An atomistic study. *Comp. Mater. Sci.*, 101:181–188, 2015.

12. Benjamin Spencer, Yongfeng Zhang, Pritam Chakraborty, S. Bulent Biner, Marie Backman, Brian Wirth, Stephen Novascone, and Jason Hales. Grizzly year-end progress report. INL/EXT-13-30316, Idaho National Laboratory, September 2013.

13. P. Chakraborty, S. B. Biner, Y. Zhang, and B. Spencer. Crystal plasticity model of reactor pressure vessel embrittlement in Grizzly. , Idaho National Laboratory, July 2015.

14. Y. Zhang, D. Schwen, H. Ke, X. Bai, and J. Hales. Mesoscale modeling of solute precipitation and radiation damage. , Idaho National Laboratory, September 2015.

15. S. Plimpton, C. Battaile, M. Chandross, L. Holm, A. Thompson, V. Tikare, G. Wagner, E. Webb, X. Zhou, C. Garcia Cardona, and A. Slepoy. Crossing the mesoscale no-man's land via parallel kinetic monte carlo. , Sandia National Laboratory, October 2009.

16. Benjamin Spencer, Yongfeng Zhang, Pritam chakraborty, Marie Backman, William Hoffman, Daniel Schwen, S. Bulent Biner, and Xianming Bai. Grizzly status report. , Idaho National Laboratory, September 2014.

17. E. Vincent, C. S. Becquart, and C. Domain. Microstructural evolution under high flux irradiation of dilute Fe-CuNiMnSi alloys studied by an atomic kinetic monte carlo model accounting for both vacancies and self interstitials. *J. Nucl. Mater.*, 382:154–159, 2008.

18. K. Farrell, T. S. Byun, and N. Hashimoto. Deformation mode maps for tensile deformation of neutron-irradiated structural alloys. *Journal of Nuclear Materials*, 335:471, 2004.

19. F. Christien and A. Barbu. Modelling of copper precipitation in iron during thermal aging and irradiation. *Journal of Nuclear Materials*, 324:90, 2004.

20. S. I. Golubov, A. M. Ovcharenko, A. V. Barashev, and B. N. Singh. Grouping method for the approximate solution of a kinetic equation describing the evolution of point-defect clusters. *Philosophical Magazine A*, 81(3):643–658, 2001.

21. Frederic Soisson and Chu-Chun Fu. Cu-precipitation kinetics in α-fe from atomistic simulations: Vacancy-trapping effects and cu-cluster mobility. *Phys. Rev. B*, 76:214102, 2007.

22. X. Hu, D. Xu, T. S. Byun, and B. D. Wirth. Modeling of irradiation hardening of iron after low-dose and low-temperature neutron irradiation. *Modelling and Simulation in Materials Science and Engineering*, 22:065002, 2014.

23. P. Chakraborty and S. B. Biner. Crystal plasticity modeling of irradiation effects on flow stress in pure-iron and iron-copper alloys. *Mechanics of Materials*, 101:71–80, 2016.

24. C. H. Ersland, I. R. Vatne, and C. Thaulow. Atomistic modeling of penny-shaped and through-thickness cracks in bcc iron. *Modelling Simul. Mater. Sci. Engg.*, 20:075004, 2012.

25. C. G. Schmidt and A. K. Miller. The effect of solutes on the strength and strain hardening behavior of alloys. *Acta Metallurgica*, 30:615–625, 1982.

26. S. Kotrechko, V. Dubinko, N. Stetsenko, D. Terentyev, X. He, and M. Sorokin. Temperature dependence of irradiation hardening due to dislocation loops and precipitates in RPV steels and model alloys. *Journal of Nuclear Materials*, 464:6–15, 2015.

27. E. Kuhl, P. Steinmann, and I. Carol. A thermodynamically consistent approach to microplane theory, Part II. Dissipation and inelastic constitutive modeling. *Int. J. Solids Struct.*, 38:2933–2952, 2001.

28. Z. P. Bazant and B. H. Oh. Efficient numerical integration on the surface of a sphere. *Z. angrew. Math. n. Mech.*, 66:37–49, 1986.